JGR Space Physics

RESEARCH ARTICLE
10.1029/2022JA030317

The Effects of Solar Cycle Variability on Nanodust Dynamics in the Inner Heliosphere: Predictions for Future STEREO A/WAVES Measurements

A. R. Poppe[1] and **C. O. Lee**[1]

[1]Space Sciences Laboratory, University of California at Berkeley, Berkeley, CA, USA

Key Points:

- Inner heliospheric nanodust dynamics are modeled over a broad range of solar cycles and IMF polarity
- Cessation of single-hit impacts on STA/WAVES is correlated with model predictions of declining nanodust fluxes at 1 au
- We predict single-hit impacts due to nanodust impacts should gradually reappear in STA/WAVES between 2022 and 2028

Supporting Information:

Supporting Information may be found in the online version of this article.

Correspondence to:

A. R. Poppe,
poppe@berkeley.edu

Citation:

Poppe, A. R., & Lee, C. O. (2022). The effects of solar cycle variability on nanodust dynamics in the inner heliosphere: Predictions for future STEREO A/WAVES measurements. *Journal of Geophysical Research: Space Physics*, *127*, e2022JA030317. https://doi.org/10.1029/2022JA030317

Received 24 JAN 2022
Accepted 20 APR 2022

Author Contributions:

Conceptualization: A. R. Poppe, C. O. Lee
Formal analysis: A. R. Poppe, C. O. Lee
Funding acquisition: A. R. Poppe, C. O. Lee
Methodology: A. R. Poppe, C. O. Lee
Project Administration: A. R. Poppe, C. O. Lee
Software: A. R. Poppe, C. O. Lee
Validation: A. R. Poppe, C. O. Lee
Writing – review & editing: A. R. Poppe, C. O. Lee

Abstract The collisional grinding of interplanetary meteoroids should continually produce grains over a wide range of sizes, including down to the nanometer-size regime. Once generated, nanodust grains are subject to interplanetary electromagnetic forces from the solar wind due to their relatively large charge-to-mass ratios, resulting in complex and highly time-dependent dynamics. Here, we use the coupled Wang-Sheeley-Arge solar corona and Enlil solar wind models together with a nanodust charging and dynamics model to explore the behavior and variability of nanodust dynamics in the inner heliosphere (<1 au) both within and across multiple solar cycles. In particular, we quantify the relative accessibility of these grains to 1 au across solar cycles 23 and 24, including focusing and defocusing heliospheric conditions. Finally, we qualitatively compare our model results with STEREO A (STA)/WAVES observations and identify correlations between the STA/WAVES single-hit rate and the relative flux of >10 nm grains. Using solar cycle 23 as a proxy for the behavior of solar cycle 25, since both solar cycles share the same defocusing-to-focusing transition, we predict the relative flux of nanodust grains in the future and identify times at which nanodust impacts may reappear in the STA/WAVES data set. Continued analysis of future STA/WAVES observations will provide an important test of this prediction, either bolstering or weakening the interpretation of electromagnetically accelerated nanodust grains as the source of single-hit events in the STA/WAVES Time Domain Sampler data set.

1. Introduction

Based on numerous observations and concurrent modeling, interplanetary dust in the inner heliosphere is believed to originate from a variety of sources, including short-period comets such as Jupiter-family comets, long-period comets such as Halley-type and Oort Cloud comets, and asteroids in the main belt (e.g., Nesvorný et al., 2010, 2011a, 2011b; Pokorný et al., 2014; Rigley & Wyatt, 2022; Rowan-Robinson & May 2013). In the outer solar system and heliosphere, dust production from the Edgeworth-Kuiper Belt (EKB) is believed to provide the dominant source of dust grains there, with some indications that EKB grains may also contribute to the flux in the inner heliosphere (e.g., Landgraf et al., 2002; Liou et al., 1996; Poppe et al., 2019). The presence of interplanetary dust in the inner heliosphere contributes to several physical phenomena. Deep within the heliosphere, scattered sunlight and thermal reradiation contributes to the formation of the solar F-corona (e.g., Kimura & Mann, 1998; Mann, 1992; Stenborg & Howard, 2017). Studies of the F-corona have long sought evidence of a "dust-free" region close to the Sun due to dust grain sublimation or collisional destruction, and recent Parker Solar Probe observations have provided preliminary evidence suggesting such a region does in fact exist (Howard et al., 2019). Additionally, inner-heliospheric dust grains interact with the solar wind ion distributions via multiple processes, leading to the formation of inner-source pickup ions (e.g., Geiss et al., 1995; Schwadron et al., 2000; Quinn et al., 2018). Such pickup ions are recognized are one possible seed source for observed anomalous cosmic rays (ACRs) in the heliosphere (e.g., Schwadron & Gloeckler, 2007). Thus, a full description of the physical and dynamical evolution of interplanetary dust grains is critical for understanding the full nature of the inner heliosphere.

As interplanetary micrometeoroids orbit around the Sun, they also undergo erosive and destructive collisions with each other, a so-called "collisional cascade" that generates daughter particles over a wide range of radii, including into the nanometer-size regime (e.g., Borkowski & Dwek, 1995; Stark & Kuchner, 2009; Szalay et al., 2021). Multiple spacecraft observations of impact-related phenomena have been interpreted as being due to a flux of nanometer-sized interplanetary dust grains that have been accelerated to a significant fraction of typical solar wind speeds due to their presumed large charge-to-mass ratio (e.g., Le Chat et al., 2013; Meyer-Vernet

et al., 2016; Meyer-Vernet, Maksimovic, et al., 2009; Schippers et al., 2014, 2015; Zaslavsky et al., 2012). To date, however, we do not yet fully understand the production mechanisms and subsequent dynamics of such nanometer-sized dust grains in the inner heliosphere. In turn, this lack of understanding has led to continued discussion in the literature presenting arguments both for (e.g., Meyer-Vernet, Maksimovic, et al., 2009; Pantellini et al., 2012; Zaslavsky et al., 2012) and against (Kellogg et al., 2018) the interplanetary of such signals as results from high-speed nanodust.

In a previous study (Poppe & Lee, 2020), we investigated the dynamics of nanodust grains between 1 and 30 nm in the inner heliosphere using a combination of the WSA-Enlil solar corona-solar wind model (Arge et al., 2004; Arge & Pizzo, 2000; Odstrcil, 2003) and a nanodust dynamics model. This investigation focused on Carrington Rotations (CRs) 2052−2060 (∼January to September 2007), overlapping with the initial period of the STEREO mission (Kaiser et al., 2008). The model results quantified the degree of structure in nanodust grain fluxes in the inner heliosphere primarily as a function of grain size. In agreement with previous analytical and computational investigations (e.g., Czechowski & Mann, 2010, 2012; Ip & Yan, 2012; Juhász & Horányi, 2013), we found that nanodust grains can be accelerated to a significant fraction of the solar wind speed (∼hundreds of km/s) and that the heliospheric current sheet plays an important role in guiding nanodust grains through the inner heliosphere via the process of "current sheet surfing," We also found that for CRs 2052–2060, each individual CR had approximately an order-of-magnitude variation in detectable nanodust fluxes at 1 au as a function of heliocentric longitude due to the underlying presence of varying slow wind and fast wind structures. Despite this variation within an individual CR, the modeled fluxes over this ∼8 month period did not drastically change, at least in a qualitative sense.

Using these model results, we predicted the flux of observable nanodust grains to the STEREO A and B spacecraft as a function of time within CRs 2052–2060 and compared these predictions to observed "single-hit" impact rates on the Time Domain Sampler (TDS) subsystem of the STEREO A and B WAVES instruments (Zaslavsky et al., 2012). As discussed in depth in the previous literature (e.g., Meyer-Vernet, Maksimovic, et al., 2009; Pantellini et al., 2012; Zaslavsky et al., 2012), these single-hit events are believed to be due to high-velocity (∼100's km/s) nanodust grains, despite suggestions otherwise (Kellogg et al., 2018). Our data-model comparison showed a distinct lack of agreement, especially for STEREO A, which recorded intermittent, ∼100-day long bursts of single-hits followed by long periods of nearly no hits. We suggested that the most likely source of the disagreement was our assumption of a constant production rate of nanodust grains in the inner heliosphere. Nanodust production may in fact be highly aperiodic and bursty, generated by processes such as asteroidal and/or cometary disruption (e.g., Granvik et al., 2016; Ip & Yan, 2012), or changes in inner coronal magnetic topology (e.g., Czechowski & Mann, 2012). Indeed, recent results from the Parker Solar Probe indicate that the collisional evolution of slightly larger, submicron-sized grains (i.e., ∼100−300 nm) in the inner zodiacal cloud is more structured and time-variable than previously understood likely due to the presence of discrete meteoroid streams (e.g., the Geminids) that increase the local collisional rate along their respective orbits (Malaspina et al., 2020; Pusack et al., 2021; Szalay et al., 2021).

Despite the lack of agreement between the modeled nanodust fluxes and the STEREO/WAVES observations in our previous study, it is still critical to understand the variation in nanodust dynamics in the inner heliosphere, in particular as a function of solar cycle. As shown in Figure 1 and discussed in previous work (e.g., Czechowski & Mann, 2010; Juhász & Horányi, 2013), the first-order behavior of nanodust grains in the inner heliosphere is governed by the polarity of the solar magnetic dipole moment and by extension, the global morphology of the interplanetary magnetic field (IMF). During focusing conditions, the interplanetary convective electric field points generally toward the heliospheric current sheet (HCS), thereby driving charged nanodust grains toward the HCS as well. Grains that pass through the HCS into an oppositely oriented IMF sector are then exposed to an oppositely pointing convective electric field, which acts to restore their motion back toward the HCS. By this method (sometimes referred to as HCS "surfing"), nanodust grains stay near the heliographic equator and are thus more likely to be observed at greater heliocentric distances. In contrast, defocusing conditions are such that the polarity of the IMF and interplanetary convective electric field are reversed. Nanodust grains are then driven away from the HCS to high heliographic latitudes and generally do not encounter the HCS. Despite our current understanding, a fully consistent model for the degree of variation in inner-heliospheric nanodust fluxes over both solar cycles and focusing-to-defocusing transitions has not yet been reported.

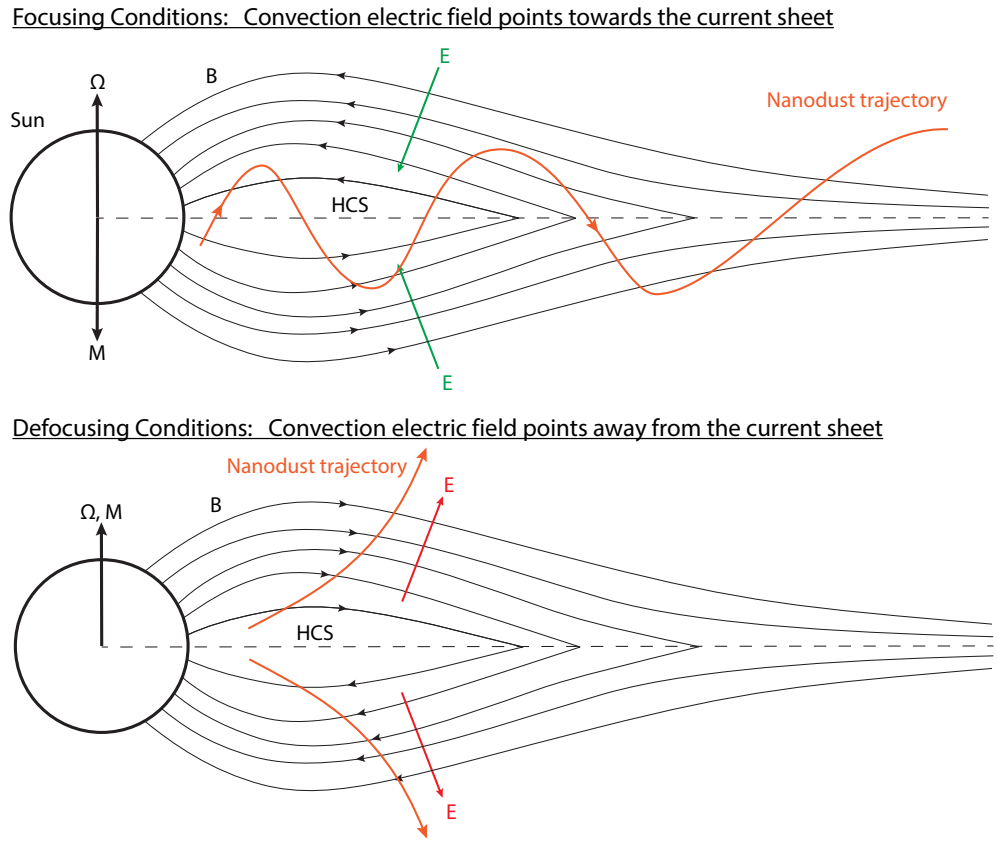

Figure 1. A cartoon illustrating the basic field geometry and motion of nanodust grains in the inner heliosphere for (top) focusing and (bottom) defocusing conditions.

Here, we continue to explore the dynamics of inner-heliospheric nanodust grains using the modeling framework developed in Poppe and Lee (2020), focusing in particular on the variability in nanodust dynamics as a function of both solar cycle and focusing or defocusing interplanetary magnetic fields. In contrast to our previous study, however, we do not make an attempt to calculate "absolutely calibrated" nanodust fluxes to the STEREO spacecraft (or any other object). Given our lack of understanding of both the rates and spatial distributions for the production of nanodust grains and the specific instrumental response of STEREO/WAVES to high-velocity nanodust impacts, we instead focus on the relative "accessibility" of nanodust grains from the inner heliosphere out to 1 au. Also, note that due to the failure and loss of the STEREO B spacecraft, we do not analyze and/or predict future nanodust fluxes to STB, given that such predictions are moot. In Section 2, we describe both the WSA-Enlil and nanodust dynamics models used in this study. In Section 3, we present results from the modeling, including nanodust dynamics across two neighboring solar cycles, 23 and 24, in Section 3.1, a comparison of STA/WAVES TDS nanodust hits and the nanodust model results in Section 3.2 and a prediction for future STA/WAVES TDS measurements in solar cycle 25 using the nanodust model in Section 3.3. Finally, Section 4 discusses the broader implications of our results and concludes.

2. Model Description

Figure 2 shows the HCS tilt angle and the strength of the solar axial dipole as a function of time, spanning CRs 1780–2255 (covering the approximate timespan 1987–2021). This timespan encompasses most of solar cycle 22, all of solar cycles 23 and 24, and the beginning years of solar cycle 25. During each solar cycle, the HCS tilt angle starts at relatively low inclinations, $<\sim 10°$, coinciding with solar minimum. Progressing past solar minimum, the HCS tilt rises sharply, typically reaching $>70°$ within approximately 3 years. Past solar maximum, the HCS tilt declines more slowly than its corresponding rise, typically taking another 6–8 years to fall to back down to its minimum value at the next solar cycle minimum. In addition to the magnitude of the HCS tilt, the sign of

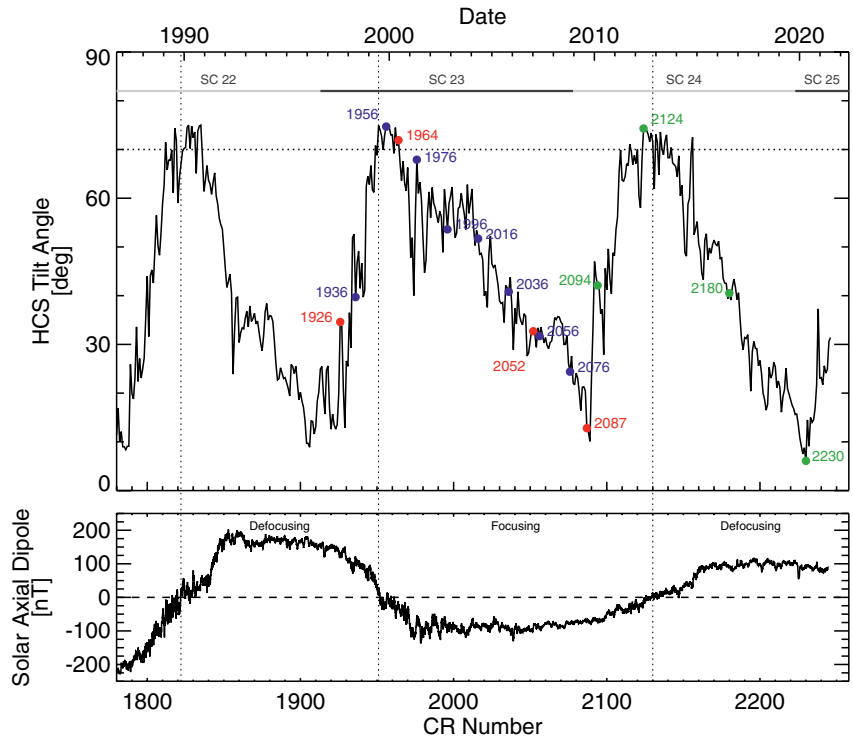

Figure 2. (top) The heliospheric current sheet (HCS) tilt angle as a function of time, in both Carrington Rotations (CRs) and year. Horizontal gray and black bars denote the extent of solar cycles 22–25. Selected CRs used in the nanodust modeling are denoted by various colored dots, as discussed in the text. (bottom) The strength of the solar axial dipole as a function of time, with focusing and defocusing periods labeled.

the solar axial dipole moment clearly distinguishes focusing periods that possess negative axial dipole moments, and defocusing periods that possess positive axial dipole moments (see also Figure 1). Transitions between these periods occur approximately at CRs 1822 (focusing → defocusing), 1950 (defocusing → focusing), and 2130 (focusing → defocusing). The next defocusing-to-focusing transition should occur near solar cycle 25 maximum, roughly in the 2023–2025 timeframe.

Denoted in colors (green, red, blue) are specific CRs for which we have modeled nanodust dynamics for our current study. For reference, our previous study (Poppe & Lee, 2020) modeled nanodust dynamics from CRs 2052–2059 near the start of the STEREO mission. In red are four CRs during solar cycle 23, representing distinct phases of the solar cycle: rising phase (CR 1926), solar maximum (CR 1964), declining phase (CR 2052), and solar minimum (CR 2087; on the boundary with solar cycle 24). In green are four additional CRs during solar cycle 24 (2094, 2124, 2180, 2230) that possess similar HCS tilt angle magnitude but opposite polarity compared to the solar cycle 23 CRs in red. Finally, in blue are eight evenly spaced CRs through solar cycle 23 (1936, 1956, 1976, 1996, 2016, 2036, 2056, and 2076) that straddle the defocusing-to-focusing transition that occurred near CR 1950. A similar defocusing-to-focusing transition is expected in the upcoming solar cycle 25, and thus, we use these eight CRs to model and predict the behavior of nanodust grains during solar cycle 25 in Section 3.3. We include in this prediction the times at which nanodust grains of various sizes should be theoretically accessible to STEREO A at 1 au and potentially detected by the STA/WAVES instrument.

To model the dynamics of nanodust grains in the inner heliosphere, we used an identical approach to that from Poppe and Lee (2020), which combined the WSA-Enlil solar corona-solar wind model and a nanodust charging and dynamics model. While the full details of the modeling approach are found in Poppe and Lee (2020), we provide a brief synopsis here. For each CR chosen for this study, we used the National Aeronautics and Space Administration (NASA) Community Coordinated Modeling Center (CCMC) Runs-on-Request service (available publicly at https://ccmc.gsfc.nasa.gov/requests/requests.php) to run and obtain WSA-Enlil model results. The results for each CR were visually inspected and validated before continuing (see Supporting Information S1).

Note that during this validation process, it was determined that WSA-Enlil results for CR 2036 were invalid due to missing photospheric maps. Thus, we replaced CR 2036 with the neighboring CR 2035. For convenience, we still refer to this CR as 2036 throughout the paper. The WSA-Enlil model output (i.e., heliospheric magnetic fields, solar wind density, velocity, and temperature) was then used as input to the nanodust dynamics model.

For each modeled CR, the nanodust dynamics model tracked 500,000 nanodust grains at each of 10, logarithmically spaced size bins spanning 1–30 nm radius. The interplanetary dust density distribution, $n(r)$, was adopted from the "fan-model" from Leinert et al. (1976, 1981), based on rocket and Helios 1/2 zodiacal light photometry measurements, given by,

$$n(r) = r^{-1.3}\exp\left(-2.6|\sin\beta_{\odot}|\right), \tag{1}$$

where r is the heliocentric distance and $\beta_{\odot}$ is the ecliptic latitude. The collisional production distribution of nanodust grains, $\Gamma(r)$, is then given by the product of the density squared and the relative impact velocity (assumed to scale as, $v_{imp}(r) \propto r^{-0.5}$) as,

$$\Gamma(r) = n^2(r)\cdot r^{-0.5} = r^{-3.1}\exp^2\left(-2.6|\sin\beta_{\odot}|\right). \tag{2}$$

Both the interplanetary dust density and collisional production rate distributions are depicted in Figure 1 of Poppe and Lee (2020). Once each nanodust grain was initialized, the model integrated a coupled set of equations describing the grain position, velocity, and charge. Forces on the nanodust grain consisted of solar gravity appropriately reduced by the effects of solar radiation pressure (although we note that radiation pressure is very weak for grains in this size regime, Burns et al., 1979) and the electromagnetic Lorentz force. The calculation of the Lorentz force on the nanodust grain used the electric and magnetic fields interpolated from the WSA-Enlil model grid to the instantaneous position of the nanodust grain. Changes in the nanodust charge included currents from photoemission, solar wind ion and electron collection, and secondary electron emission. Similar to the electromagnetic fields, values for the solar wind ion and electron collection currents and the secondary electron emission currents used results (i.e., solar wind density, speed, temperature) interpolated from WSA-Enlil to the nanodust grain position. Under this modeling scheme, each individual grain was followed through the domain until it encountered the inner or outer radial boundaries at 0.1 and 1.0 au, respectively, or the upper or lower latitudinal boundaries at ±58°. Finally, for each nanodust grain size during each CR, the nanodust dynamics model returned the mean nanodust density, flux, and velocity distributions in the inner heliosphere.

We also note here (as similarly done in our previous study, Poppe & Lee, 2020) that certain assumptions and/or limitations exist to our modeling approach. The WSA-Enlil model is dependent on the accuracy of observations of the photospheric magnetic fields (e.g., Arge et al., 2004; Arge & Pizzo, 2000) and may be less accurate during times of high solar variability (e.g., solar flares, coronal mass ejections). Furthermore, the WSA-Enlil model does not account for any self-consistent feedback from the presence of nanodust grains, which may locally perturb the solar wind conditions (e.g., Jia et al., 2012; Lai & Russell, 2018; Rasca et al., 2014a, 2014b). For the nanodust dynamics model, we have assumed a single and time-stationary spatial distribution for the nanodust density and collisional production rates (Leinert et al., 1976, 1981), which may not strictly hold. Given the already complex nature of our model, however, we leave an exploration of varying nanodust initial distributions to future work. Finally, while the smallest nanodust grains we modeled had lifetimes from 0.1 to 1 au of between ~3 and 8 days, we have found that under some conditions, nanodust grain lifetimes last up to ~50 days, longer than an individual CR. The integration of a nanodust grain for longer than an CR-lifetime (~27 days) is not strictly valid; however, a modeling approach that continuously evolves both the nanodust grain and the WSA-Enlil results is currently computationally prohibitive, and thus, we also leave this exercise for future work. Again, further details on the modeling assumptions and limitations can be found in Section 2.3 of Poppe and Lee (2020).

3. Model Results

3.1. Solar Cycle Variability in Nanodust Fluxes

Similar to Poppe and Lee (2020), we first simulated, downloaded, and validated all WSA-Enlil simulation runs described in the previous section (see also the Supporting Information S1). Having verified these results (and replacing CR 2036 with CR 2035; see above), we then proceeded to model all 10 nanodust sizes for each selected CR modeled with WSA-Enlil. Figure 3 shows snapshots of the nanodust flux within ±7.25° latitude of the

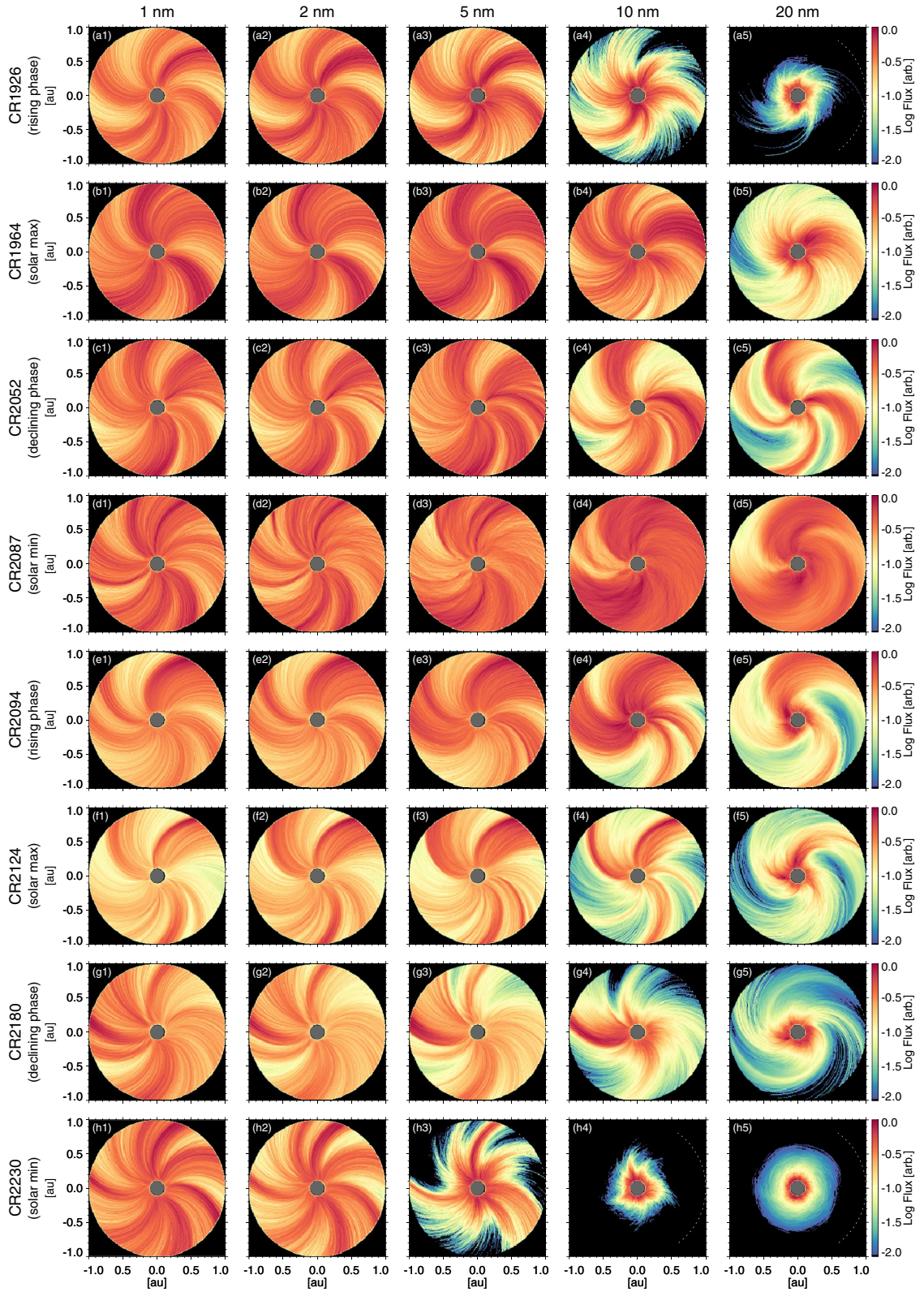

Figure 3. Snapshots of the solar-equatorial nanodust flux for five selected grain sizes (1, 2, 5, 10, 20 nm) for eight Carrington Rotations (CRs) spanning solar cycles 23 and 24. Fluxes are scaled by r^2 and each normalized to their individual maximum in order to emphasize comparative structures across sizes and CRs.

Heliocentric-Earth-Equatorial (HEEQ) equatorial plane at five selected grain sizes (1, 2, 5, 10, 20 nm) for the eight selected CRs during solar cycles 23 and 24. In order to emphasize the comparison of various structures and the relative accessibility of grains to 1 au, all fluxes are scaled by r^2 (where r is the heliocentric distance) and each panel is normalized to its own respective maximum. By inspection of the columns in Figure 3, one can easily see that nanodust fluxes for the smallest grain sizes of 1 and 2 nm show little qualitative variation over both solar cycles 23 and 24, although the fluxes during any individual CR have variable azimuthal structure due to the specific variations in the underlying solar wind structure (e.g., slow versus fast wind sectors). In comparison, the flux of 5, 10, and 20 nm grains show increasingly variable structure and accessibility to 1 au over time.

For CR 1926, panels 3(a1–a5), which occurs near the beginning of solar cycle 23 with defocusing polarity, the flux of nanodust grains near the heliographic equator is increasingly suppressed as a function of grain size. The 10 nm grains have only limited azimuthal sectors where relative fluxes at 1 au are greater than 10^{-2} while the 20 nm grains have close to no relative fluxes larger than 10^{-2} at 1 au. For CR 1964 (solar max), panels 3(b1–b5), the 1, 2, and 5 nm fluxes appear qualitatively similar to those in CR 1926, with moderate azimuthal structure and sustained flux reaching 1 au. The 10 nm flux also appears similar to the smaller grain sizes during this CR. For the 20 nm grains, fluxes are intermediate between those of CR 1926 and CR 2052. Due to the large HCS tilt angle at solar maximum (e.g., see Figure 2), grains that are subjected to only a single IMF sector as they are accelerated outwards tend to be fully driven away from the HEEQ equatorial plane, while those grains that happen to undergo an HCS crossing partway through their acceleration outwards will be driven back toward the HEEQ equatorial plane and thus, stand a greater chance of arriving at 1 au within ±7.25° HEEQ latitude. For CR 2052, panels 3(c1–c5), the fluxes are identical to those presented previously in Figure 5 of Poppe and Lee (2020), showing imprints of the underlying Parker-spiral structure onto the nanodust grain fluxes as they are accelerated outwards, now under the presence of focusing-polarity fields. As sizes increase, the degree of structure seen in the nanodust fluxes increases as larger-sized grains more closely follow the HCS tilt, thereby drifting to higher HEEQ latitudes and out of the ±7.25° HEEQ latitude range shown here. During CR 2087 (solar min), panels 3(d1–d5), nanodust grain fluxes across all sizes are particularly high relative to the other modeled CRs. Since CR 2087 has a very low HCS tilt with focusing polarity, nanodust grains can continually surf the HCS and remain close to the HEEQ equatorial plane out to and past 1 au. For the smaller grains, small-scale, Parker-spiral-like structures are present in the flux, reflecting underlying variations in the solar wind structure. As grain sizes increase to 10 and 20 nm, these features blend together as the nanodust grains take longer to progress to 1 au and are subject to a broader range of underlying solar wind and IMF conditions. Proceeding into solar cycle 24 with CRs 2094 (rising phase), 2124 (solar max), 2180 (declining phase), and 2230 (solar min), the trends seen in the nanodust grains fluxes during solar cycle 23 gradually reverse. Nanodust fluxes at the largest sizes diminish earlier in the solar cycle, increasingly so after the transition from focusing-to-defocusing polarity that occurs near CR 2124. A greater degree of azimuthal structure emerges in the 5, 10, and 20 nm nanodust grain fluxes in CRs 2094, 2124, and 2180, similar to that seen in CR 2052 in solar cycle 23. At solar minimum, CR 2230, the 5, 10, and 20 nm nanodust grain fluxes are the lowest over all modeled CRs with only limited fluxes of 5 nm grains at 1 au at the 10^{-2} level and no fluxes of either 10 or 20 nm grains at 1 au at the 10^{-2} level.

In addition to the relative variability in the two-dimensional nanodust grain fluxes in the inner heliosphere, we can also inspect the radial distribution of nanodust grain fluxes across CRs. Figures 4a and 4b show the azimuthally averaged radial variation of nanodust fluxes within 1 au for 1 and 30 nm nanodust grains, respectively. In contrast to Figure 3, the radial flux curves in Figure 4 are normalized to the highest flux at each individual size across all CRs, thereby allowing a comparison of relative fluxes across CRs. Note that nanodust grains are only generated at distances greater than 0.10 au (i.e., the inner Enlil boundary) and thus, fluxes are not generally expected within 0.10 au (denoted by the gray-shaded region). For 1 nm grains, Figure 4a clearly shows very little variation in relative fluxes across solar cycles 23 and 24. The 1 nm fluxes always peak between 0.1 and 0.125 au with a rapid drop inwards of ∼0.13 to 0.10 au (again, due to the presence of the inner Enlil boundary at 0.10 au) and a more gradual decline outwards. At 1 au, variation in the 1 nm fluxes over all CRs is at most a factor of ∼2. In contrast, Figure 4b shows that the 30 nm fluxes vary significantly over time. The peaks in the 30 nm fluxes over all CRs are all located near ∼0.13 au, similar to the 1 nm fluxes; however, the overall magnitude of the 30 nm peak flux at 0.13 au varies by a factor of ∼5 from CR 2087 to CRs 1926 and 2230. Outwards of 0.13 au, the 30 nm fluxes decline as a function of heliocentric distance, albeit at differing rates. CR 2087 maintains the highest 30 nm flux at all distances within 1 au, while CRs 1926 and 2230 have the lowest (and nearly identical) fluxes across all distances. All other CRs fall in between these two extremes with slightly different heliocentric

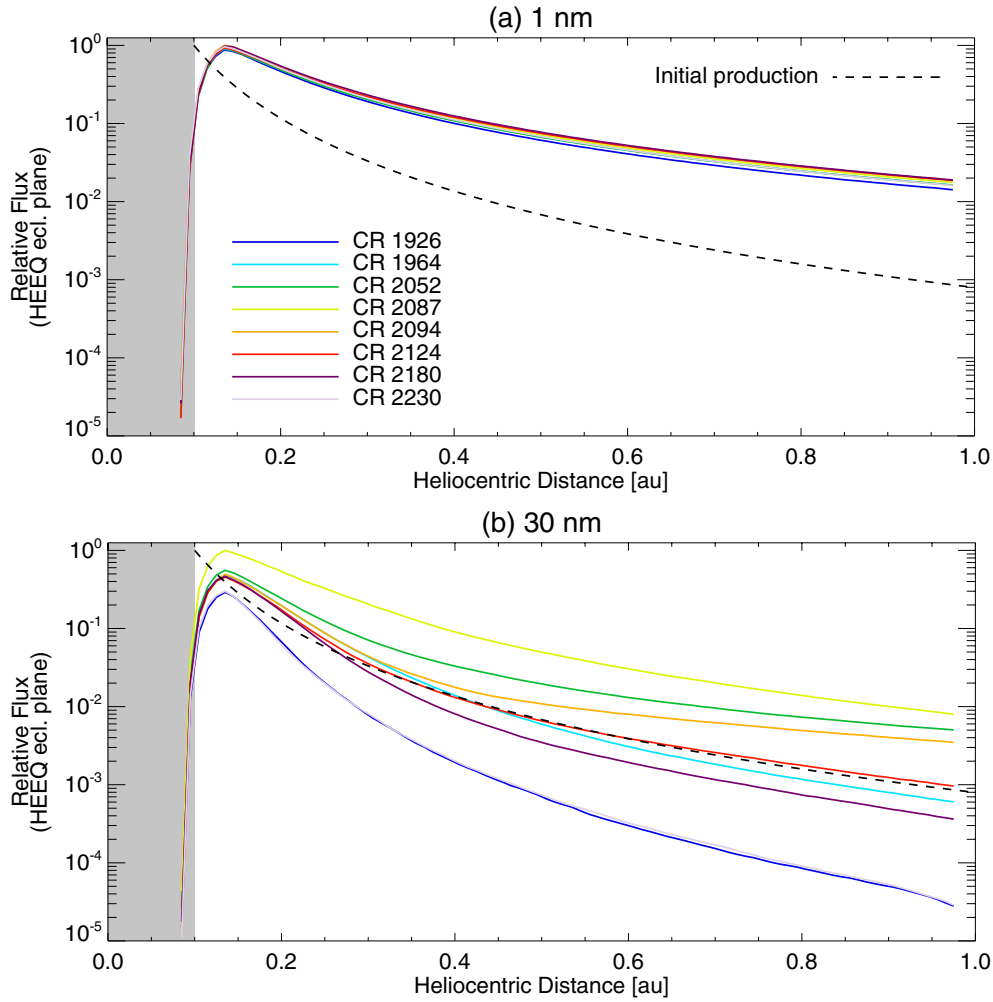

Figure 4. The azimuthally averaged flux as a function of heliocentric distance for (a) 1 nm and (b) 30 nm for eight Carrington Rotations (CRs) spanning solar cycles 23 and 24. Curves for each size are normalized to the maximum flux over all CRs. The black dashed line denotes the relative, initial collisional production rate of nanodust grains as a function of heliocentric distance, for comparison.

behavior. Nevertheless at 1 au, the divergence of the 30 nm fluxes yields more than two orders-of-magnitude variability, highlighting again the strong effect that the IMF polarity (i.e., focusing or defocusing) has on larger-sized nanodust grains.

3.2. Comparison to STEREO A/WAVES

With two full solar cycles of modeled nanodust grain flux variability in hand, we now make a comparison to the observed single-hit TDS events reported from the STA/WAVES instrument between 2007 and 2013 (Zaslavsky et al., 2012). We make this comparison with the full understanding that the response mechanism of the STEREO/WAVES instruments to high-velocity nanodust grains is poorly understood and apparently different between STEREO A and B, likely due to their opposite attitude with respect to the nanodust grain fluxes (e.g., see Meyer-Vernet, Lecacheux, et al., 2009). We also reiterate that per our previous study (Poppe & Lee, 2020), we found that the episodic nature of the observed single-hits on STEREO A suggested a strong degree of variability in the initial production of nanodust grains themselves in the inner heliosphere, something we do not model here. Thus, this comparison primarily pertains to whether or not nanodust grain fluxes can access 1 au at a given point in time, *not* whether STEREO/WAVES will definitively experience nanodust grain impacts at such times.

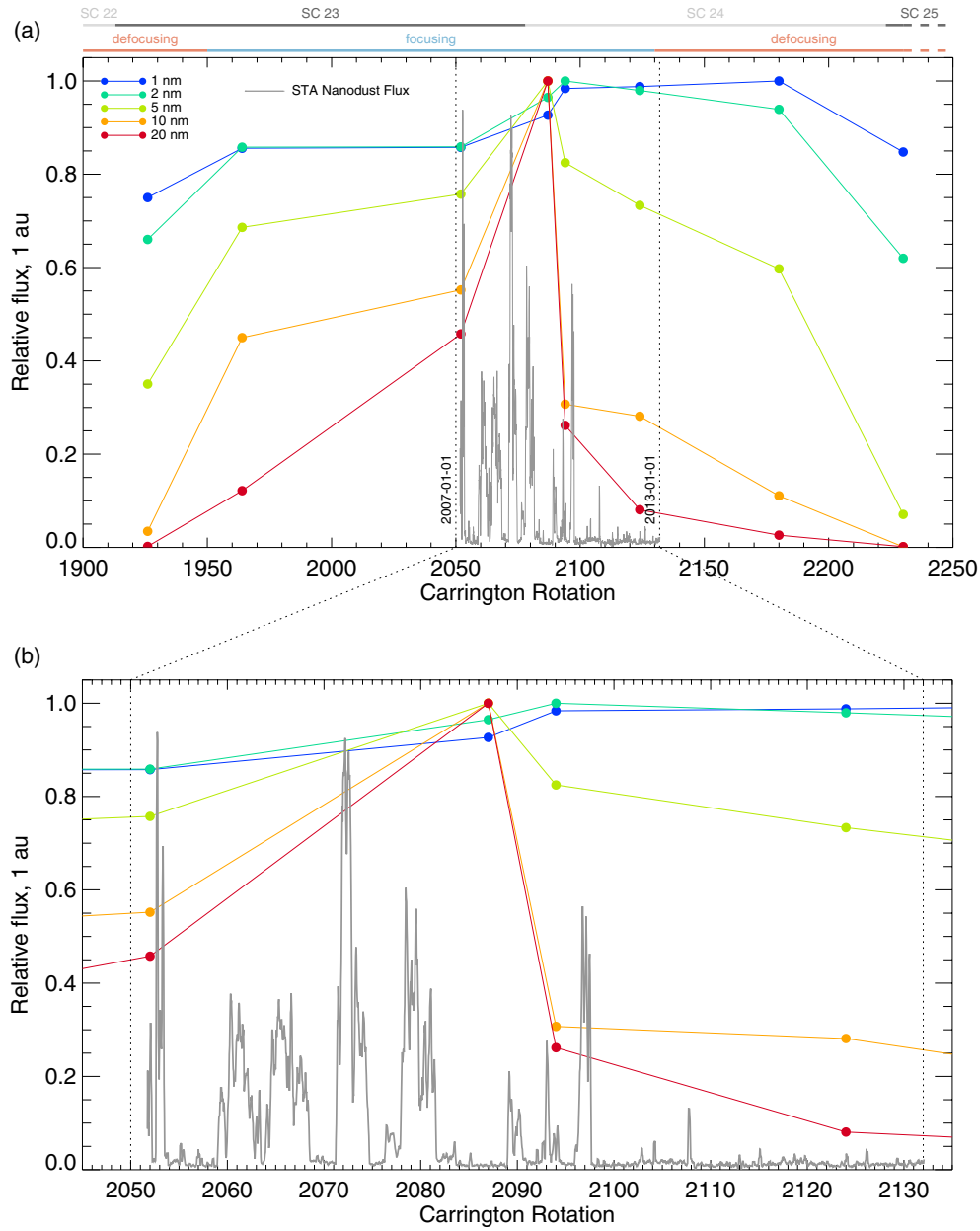

Figure 5. (a) The relative, azimuthally averaged nanodust grain flux at 1 au within ±7.25° latitude for five selected grain sizes (1, 2, 5, 10, 20 nm) as a function of Carrington Rotation. Overplotted in gray are the relative STEREO A/WAVES TDS single-hit rate from Zaslavsky et al. (2012) between 1 January 2007 and 1 January 2013. (b) Similar to panel (a), but zoomed into CRs 2045–2135.

Additionally, we note again that we do not make a comparison and prediction for STB/WAVES due to the loss of the STEREO B spacecraft.

Figure 5a shows the azimuthally averaged relative flux of nanodust grains for five sizes (1, 2, 5, 10, and 20 nm) at 1 au for the eight Carrington rotations modeled here for solar cycles 23 and 24. The flux for each grain size is individually normalized to its respective maximum across time (the respective maxima occur at CR 2180 for 1 nm, CR 2094 for 2 nm, and CR 2087 for 5, 10, and 20 nm grains). Labeled bars at the top of Figure 5a denote the various solar cycles and focusing/defocusing polarity. As discussed in the previous section, the relative nanodust grain fluxes have distinct behaviors in time as a function of their grain size. For the smallest two sizes, 1 nm (blue) and 2 nm (green), relative fluxes are always >75% and >60% of their maximum flux, respectively. Thus,

the fluxes of the smallest grain sizes undergo relatively limited changes across solar cycles and/or focusing or defocusing periods. In contrast, the larger sizes of 5 nm (yellow), 10 nm (orange), and 20 nm (red) have greater variability over time. At the beginning of the modeled period near CR 1926 (near the beginning of solar cycle 23), the relative nanodust fluxes at 1 au for these sizes are only 35%, 5%, and 1% of their respective maxima. As solar cycle 23 continues and the heliospheric polarity switches from defocusing to focusing (which occurs just prior to CR 1964), the relative nanodust grain fluxes for these sizes steadily increase, reaching their maxima at CR 2087. Immediately after CR 2087, however, the relative fluxes for the three larger grains sizes fall sharply, especially for the 10 and 20 nm-sized grains, which drop to ∼25% of the maximum relative flux by CR 2094. This steep decline continues through solar cycle 24 and past the focusing-to-defocusing transition near CR 2130 such that by CR 2230, the relative fluxes for the three largest grain sizes have fallen to ∼7%, <1%, and <1%, respectively.

In addition to the modeled relative fluxes, we have highlighted the region of CR 2045–2135 during the beginning of the STEREO mission in panel 5(b) and overplotted the STA/WAVES single-hit rate as reported by Zaslavsky et al. (2012). These data span CRs 2052 to 2132, corresponding to the 6-year time period of 1 January 2007 to 1 January 2013. As noted in previous work (e.g., Meyer-Vernet, Lecacheux, et al., 2009; Zaslavsky et al., 2012), the STA/WAVES single-hit detection rate is characterized by a very low rate punctuated by ∼50−100 days long, episodic bursts of relatively high count rates. These bursts occur throughout the first several years of the STEREO A mission, up until approximately mid-2010 near CR 2100, where the intensity and frequency of the bursts rapidly diminish. This decline occurs near the end of solar cycle 23 (CR 2078) but somewhat prior to the focusing-to-defocusing transition near CR 2130. By comparing the modeled relative nanodust fluxes with the STA/WAVES single-hit detection rate, one sees that the abrupt end to the presence of bursts in the STA/WAVES data coincides closely with the sharp drop in relative nanodust grain fluxes of 10 and 20 nm grains. Only a few smaller bursts appear in the STA/WAVES data set after CR 2100, near CRs 2103, 2104, and 2108.

While keeping in mind the axiom that *correlation does not necessarily imply causation*, we nevertheless suggest that the drop in modeled nanodust grain fluxes at 1 au for grains >10 nm and the disappearance of single-hit bursts in STA/WAVES are related. From the modeling perspective, the underlying cause in the rapid drop in >10 nm nanodust fluxes from CR 2087 to CR 2094 (a span of only ∼6 months) is driven by the rapid change in HCS tilt across this time period. As shown in Figure 2, the HCS tilt at CR 2087 is near its overall minimum at ∼13° while the tilt at CR 2094 has increased to ∼42° only seven CRs later (∼6 months). While this change in HCS tilt does not affect the ability of smaller grains to reach 1 au (e.g., Juhász & Horányi, 2013), it does significantly impact the flux of larger grains as they are driven away from the equatorial HEEQ plane before reaching 1 au radial distance. In other words, the larger-sized nanodust grains are particularly sensitive to the changes in the magnitude of the HCS tilt and can only access 1 au during a relatively narrow window in time during a focusing/defocusing cycle.

Correlations between the individual modeled grain sizes and the appearance of single-hit bursts on STA/WAVES also provides an opportunity to constrain the primary size of impactors potentially responsible for the single-hit signals in the WAVES data set. To a relatively high degree of confidence, we can exclude 1 and 2 nm grains as contributing significantly to the single-hit flux at STEREO A, since neither of these two smaller grain sizes show a steep drop in accessibility to 1 au past CR 2100 when the STEREO A bursts diminish and disappear. The 5 nm grain flux undergoes a ∼20% decline in flux from its maximum at CR 2087 to times past CR 2090; however, such a moderate decline in accessibility does not fully capture the near-total drop in STEREO A bursts near CR 2100. In contrast, the 10 nm and especially the 20 nm grain fluxes to 1 au undergo sharp declines very near the last observed large burst on STEREO A (near CR 2097), with declines that mirror the continued lack of STEREO A bursts past CR 2100. Thus, from a correlative viewpoint, the modeling suggests that STEREO A is likely most sensitive to nanodust grains at the 10–20 nm size range, if not larger. In comparison, Zaslavsky et al. (2012) (see their Figure 6 and associated discussion) estimated that the single-hit events on STA/WAVES were most likely caused by grains in the size range of ∼3−10 nm. At the lower end of this estimated range, our modeled 3 nm grains (not shown in Figure 5 but straddling the behavior of the 2 and 5 nm grains) do not share the same time variability as the observed STA/WAVES TDS single-hit event rate, and thus, we would tend to disfavor 3 nm-sized grains as contributors. The upper end of their estimated size range, ∼10 nm, does have modeled fluxes that correlate well with the STA/WAVES single-hit impact rate as discussed above.

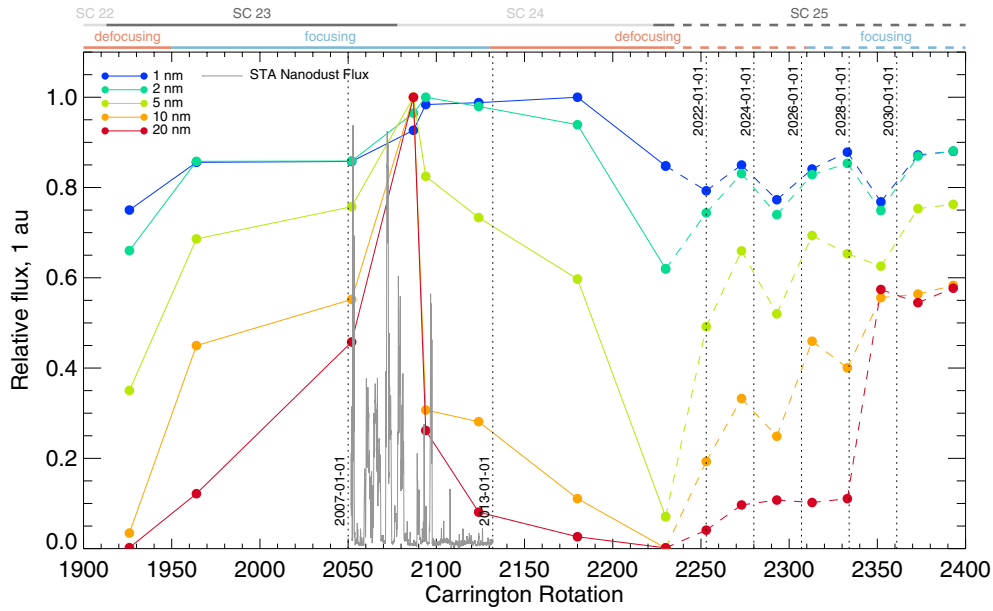

Figure 6. The relative, azimuthally averaged nanodust grain flux at 1 au within ±7.25° latitude for five selected grain sizes (1, 2, 5, 10, 20 nm) as a function of Carrington Rotation. Solid lines denote Carrington Rotations (CRs) modeled with actual solar photospheric map observations in the past (see also Figure 5a), while dashed lines represent predicted CRs modeled by using analogous photospheric maps from SC 23 (see text for full description). The relative STEREO A WAVES single-hit rate is overplotted in gray (see also Figure 5b).

3.3. Prediction for Future STEREO A/WAVES Measurements

Having explored the variability of nanodust flux accessibility to 1 au through solar cycles 23 and 24, we now turn to a prediction for future behavior in nanodust fluxes during the upcoming solar cycle 25, which began in late 2019. In particular, such an exercise will allow us to make general predictions about the dates during which nanodust impacts may be most likely to reappear in the STA/WAVES data set as single-hit events. In order to predict the general behavior of nanodust fluxes during solar cycle 25, we identified eight additional, evenly spaced Carrington rotations that occurred during solar cycle 23 (e.g., see blue points in Figure 2). Since solar cycle 23 possesses the same sense of a defocusing-to-focusing transition in the heliospheric polarity as solar cycle 25 will, we can broadly expect similar qualitative behavior in the nanodust grain flux, even if the specific conditions during any individual CR may not be identically reproduced from solar cycle 23 to solar cycle 25. To quantify this prediction, Figure 6 shows the relative flux of nanodust grains for five sizes (1, 2, 5, 10, 20 nm) at 1 au for *all* the Carrington rotations modeled here. Similar to Figure 5, the flux for each grain size is individually normalized to its respective maximum across time (CR 2180 for 1 nm, CR 2094 for 2 nm, and CR 2087 for 5, 10, and 20 nm grains). In Figure 6, the solid portion of the lines for each grain size denotes CRs that occurred in the past and thus, have actual photospheric maps with which to run WSA-Enlil (i.e., identical to that shown in Figure 5a). In contrast, the dashed portion of each line denotes the predicted relative flux for each grain size during solar cycle 25, calculated by using the corresponding solar cycle 23 maps, as described above. For context, Figure 6 also denotes the time periods of solar cycles 22, 23, 24, and 25 as the light/dark gray line, and the focusing or defocusing nature of the heliospheric fields as the red/blue line (red is defocusing, blue is focusing).

For times after CR 2230 (~April-May 2020), our predictions indicate that the smaller nanodust grain sizes of 1 and 2 nm continue at relatively constant relative fluxes near 80–90% of their respective maxima, even through the projected defocusing-to-focusing transition that should occur somewhere near CR 2310. The 5 nm relative flux recovers quickly from its overall minimum of ~7% at CR 2230 to approximately 50% at CR 2252, followed by a slow increase up to ~75% throughout solar cycle 25. The 10 nm relative flux follows a similar trend to the 5 nm flux, albeit lower in magnitude and reaching only ~60% its maximum by the end of solar cycle 25. Finally, the 20 nm relative flux does not recover quickly and remains at values ~10% of its overall maximum through CR 2343, before finally jumping significantly up to ~50–60% of its maximum by the end of solar cycle 25. Thus,

by comparison, the relative fluxes for all grain sizes at the end of the projected period (CR 2395, near 1 January 2032) have finally recovered to values similar to that seen in CR 2052 (January 2007).

The correlations between the presence of STEREO A single-hit bursts and the relative accessibility at 1 au of modeled grains at various sizes during CRs 2050–2130 offers an opportunity to predict the time at which single-hit bursts may reappear in the STA/WAVES data set. If the STEREO A single-hit observations are primarily caused by the largest modeled nanodust grains (20 nm and larger), then the drop of 20 nm flux below ∼25% near CR 2090—coincident with the disappearance of STEREO A single-hit bursts—may indicate a cutoff level below which STEREO A will not observe nanodust. Looking forward in time, the 20 nm nanodust flux at 1 au does not recover to relative values above ∼25% until approximately CR 2340, which will occur in early 2028. If STEREO A single-hits are primarily caused by slightly smaller, 10 nm grains, then one would expect nanodust grains to reappear much sooner, potentially as early as CR 2250 (early 2022), as the 10 nm relative flux rises steadily to surpass its cutoff value of ∼25% (i.e., that seen near CR 2090). If, as seems likely, STA/WAVES responds to a range of grain sizes depending on the heliospheric conditions and degree of nanodust grain acceleration, then one may expect a gradual, rather than abrupt, reappearance of single-hit events between approximately CR 2250 (early 2022) to CR 2350 (early 2028). This gradual behavior can essentially be tied back to the underlying rate of change in the HCS tilt magnitude over a solar cycle, which is asymmetric in its rising (solar minimum to solar maximum) and falling (solar maximum to solar minimum) legs (i.e., see Figure 2).

4. Discussion and Conclusion

The simulations presented here have explored the variability of inner-heliospheric nanodust grain fluxes as a function of solar wind and IMF focusing/defocusing conditions. Similar to previous numerical investigations of nanodust dynamics (e.g., Czechowski & Mann, 2010; Juhász & Horányi, 2013), our simulations show that nanodust accessibility to low HEEQ equatorial latitudes at 1 au is controlled to first order by the polarity of the interplanetary magnetic field. Focusing conditions, whereby the interplanetary electric field generally points toward the HCS, tend to allow nanodust grains to repeatedly "surf" the HCS, thereby remaining relatively close to both the ecliptic and solar-equatorial planes. In contrast, defocusing conditions, whereby the interplanetary electric field generally points away from the HCS, tend to drive nanodust grains away from the ecliptic and solar-equatorial planes, yielding less accessibility—and likely lower fluxes—at 1 au. Additionally, our simulation results show that this effect is also strongly tied to nanodust grain size. The smallest grains modeled here (typically ≤2 nm) show relatively minor variations in accessibility to 1 au over various solar cycles and focusing/defocusing conditions. This finding corresponds well with that noted in Juhász and Horányi (2013), who analytically and numerically showed that out-of-equatorial drift speeds for small grains (<∼2 nm) are much smaller than their outwards radial speeds, implying that these small grains stay near the heliographic equator out to greater heliocentric distances. In comparison, the largest grain sizes modeled here (>20 nm) show variations over two orders-of-magnitude in accessibility to 1 au over solar cycle and focusing/defocusing conditions, reflecting the sensitive dependence of the large grain sizes on the magnitude of the HCS tilt angle.

One important finding from this work is a correlation between the disappearance of single-hit event "bursts" in the STA/WAVES data set and the modeled accessibility of nanodust grains greater than 10 nm to 1 au. This correlation *suggests* that STA/WAVES is primarily responding to the impact of larger-sized, >10 nm grains, consistent with the upper size range of impactors estimated by Zaslavsky et al. (2012). For these larger grain sizes (∼10–30 nm), there in fact only exists a relatively narrow window in time, spanning CRs 2050 to 2100 (approximately November 2006 to September 2010), where our model predicts the accessibility to 1 au to be relatively high (>∼50%). It may perhaps be seen as somewhat fortuitous that the STEREO mission launched in October 2006 and began scientific operations in early 2007, just as the >10 nm nanodust grain accessibility to 1 au was peaking.

Furthermore, as discussed in Section 3.3, our simulations have allowed us to predict (albeit with only moderate accuracy) the time at which single-hit events due to nanodust grains may reappear in the STA/WAVES data sets. We emphasize again that solar wind and IMF control of inner-heliospheric nanodust fluxes is only one piece of the explanation with regards to nanodust variability in fluxes at 1 au. One must also understand the inner-heliospheric production mechanism of nanodust grains themselves, which based on recent PSP analyses, is likely to be both spatially and temporally variable (Malaspina et al., 2020; Pusack et al., 2021; Szalay et al., 2021). Depending on the specific nanodust grain size (or range of sizes) to which the STA/WAVES instrument is sensitive, the

reappearance of single-hit events may begin as early as 2022 or as late as 2028. Additionally, as opposed to the relatively sharp drop in >10 nm nanodust grain accessibility to 1 au near CR 2100, a more gradual return of nanodust accessibility is typically seen for the larger nanodust grain sizes as solar cycle 25 begins. Thus, continued monitoring of the STA/WAVES data set through solar cycle 25, along with validation of the expected dust grain fluxes with information from photospheric maps and solar wind, as they become available, offers a critical opportunity to test this prediction, thereby either bolstering or weakening the interpretation of single-hit signals in the TDS data sets as due to high-velocity interplanetary nanodust grains.

Data Availability Statement

HCS tilt angle and solar dipole data are available at http://wso.stanford.edu/Tilts.html. WSA-Enlil results are available through NASA's CCMC website. Supporting Information S1 lists the WSA-Enlil run names for each modeled CR. The nanodust dynamics flux results are available at https://doi.org/10.5281/zenodo.6415327.

Acknowledgments
The authors gratefully acknowledge support from NASA's Heliophysics Supporting Research program, Grant #80NSSC19K0830. The authors thank S. D. Bale, M. Pulupa, and A. Zaslavsky for helpful conversations regarding STEREO/WAVES, the staff at the NASA CCMC for assistance in running WSA-Enlil models and obtaining output, and T. Hoeksema for providing HCS tilt angle and solar dipole data.

References

Arge, C. N., Luhmann, J. G., Odstrcil, D., Schijver, C. J., & Li, Y. (2004). Stream structure and coronal sources of the solar wind during the May 12th, 1997 CME. *Journal of Atmospheric and Solar-Terrestrial Physics*, *66*, 1295–1309. https://doi.org/10.1016/j.jastp.2004.03.018

Arge, C. N., & Pizzo, V. J. (2000). Improvement in the prediction of solar wind conditions using near-real time solar magnetic field updates. *Journal of Geophysical Research*, *105*(A5), 10465–10479. https://doi.org/10.1029/1999JA000262

Borkowski, K. J., & Dwek, E. (1995). The fragmentation and vaporization of dust in grain-grain collisions. *The Astrophysical Journal*, *454*, 254–276. https://doi.org/10.1086/176480

Burns, J. A., Lamy, P. L., & Soter, S. (1979). Radiation forces on small particles in the solar system. *Icarus*, *40*, 1–48. https://doi.org/10.1016/0019-1035(79)90050-2

Czechowski, A., & Mann, I. (2010). Formation and acceleration of nano dust in the inner heliosphere. *The Astrophysical Journal*, *714*, 89–99. https://doi.org/10.1088/0004-637X/714/1/89

Czechowski, A., & Mann, I. (2012). Nanodust dynamics in interplanetary space. In I.Mann, N.Meyer-Vernet, & A.Czechowski (Eds.), *Nanodust in the solar system: Discoveries and interpretations, Astrophysics and Space science Library* (Vol. 385). Springer-Verlag. https://doi.org/10.1007/978-3-642-27543-2_4

Geiss, J., Gloeckler, G., & van Steiger, R. (1995). Origin of the solar wind from composition data. *Space Science Reviews*, *72*, 49–60. https://doi.org/10.1007/BF00768753

Granvik, M., Morbidelli, A., Jedicke, R., Bolin, B., Bottke, W. F., Beshore, E., et al. (2016). Super-catastrophic disruption of asteroids at small perihelion distances. *Nature*, *530*, 303–306. https://doi.org/10.1038/nature16934

Howard, R. A., Vourlidas, A., Bothmer, V., Colaninno, R. C., DeForest, C. E., Gallagher, B. et al. (2019). Near-Sun observations of an F-corona decrease and K-corona fine structure. *Nature*, *576*, 232–236. https://doi.org/10.1038/s41586-019-1807-x

Ip, W.-H., & Yan, T.-H. (2012). Injection and acceleration of charged nano-dust particles from sungrazing comets. In *Physics of the heliosphere: A 10 year retrospective* (Vol. 1436, pp. 30–35). American Institute of Physics. https://doi.org/10.1063/1.4723586

Jia, Y.-D., Ma, Y. J., Russell, C. T., Lai, H. R., Toth, G., & Gombosi, T. I. (2012). Perpendicular flow deviation in a magnetized counter-streaming plasma. *Icarus*, *218*, 895–905. https://doi.org/10.1016/j.icarus.2012.01.017

Juhász, A., & Horányi, M. (2013). Dynamics and distribution of nano-dust particles in the inner solar system. *Geophysical Research Letters*, *40*, 2500–2504. https://doi.org/10.1002/grl.50535

Kaiser, M. L., Kucera, T. A., Davila, J. M., Cyr, O. C. St., Guhathakurta, M., & Christian, E. (2008). The STEREO mission: An introduction. *Space Science Reviews*, *136*, 5–16. https://doi.org/10.1007/s11214-007-9277-0

Kellogg, P. J., Goetz, K., & Monson, S. J. (2018). Are STEREO single hits dust impacts? *Journal of Geophysical Research: Space Physics*, *123*, 7211–7219. https://doi.org/10.1029/2018JA025554

Kimura, H., & Mann, I. (1998). Brightness of the solar *F*-corona. *Earth Planets and Space*, *50*, 493–499. https://doi.org/10.1186/BF03352140

Lai, H. R., & Russell, C. T. (2018). Nanodust released in interplanetary collisions. *Planetary and Space Science*, *156*, 2–6. https://doi.org/10.1016/j.pss.2017.10.003

Landgraf, M., Liou, J.-C., Zook, H. A., & Grün, E. (2002). Origins of solar system dust beyond Jupiter. *The Astronomical Journal*, *123*, 2857–2861. https://doi.org/10.1086/339704

Le Chat, G., Zaslavsky, A., Meyer-Vernet, N., Issautier, K., Belheouane, S., Pantellini, F., et al. (2013). Interplanetary nanodust detection by the *solar terrestrial relations observatory*/WAVES low frequency receiver. *Solar Physics*, *286*, 549–559. https://doi.org/10.1007/s11207-013-0268-x

Leinert, C., Link, H., Pitz, E., & Giese, R. H. (1976). Interpretation of a rocket photometry of the inner zodiacal light. *Astronomy & Astrophysics*, *47*, 221–230.

Leinert, C., Richter, I., Pitz, E., & Planck, B. (1981). The zodiacal light from 1.0 to 0.3 AU. *Astronomy & Astrophysics*, *103*, 177–188.

Liou, J.-C., Zook, H. A., & Dermott, S. F. (1996). Kuiper belt dust grains as a source of interplanetary dust particles. *Icarus*, *124*(220), 429–440. https://doi.org/10.1006/icar.1996.0220

Malaspina, D. M., Szalay, J. R., Pokorný, P., Page, B., Bale, S. D., Bonnell, J. W., et al. (2020). Situ observations of interplanetary dust variability in the inner heliosphere. *The Astrophysical Journal*, *892*, 115. https://doi.org/10.3847/1538-4357/ab799b

Mann, I. (1992). The solar F-corona: Calculations of the optical and infrared brightness of circumsolar dust. *Astronomy & Astrophysics*, *261*, 329–335.

Meyer-Vernet, N., Lecacheux, A., Kaiser, M. L., & Gurnett, D. A. (2009). Detecting nanoparticles at radio frequencies: Jovian dust stream impacts on Cassini/RPWS. *Geophysical Research Letters*, *36*, L03103. https://doi.org/10.1029/2008GL036752

Meyer-Vernet, N., Maksimovic, M., Czechowski, A., Mann, I., Zouganelis, I., Goetz, K., et al. (2009). Dust detection by the wave instrument on STEREO: Nanoparticles picked up by the solar wind? *Solar Physics*, *256*, 463–474. https://doi.org/10.1007/s11207-009-9349-2

Meyer-Vernet, N., Moncuquet, M., Issautier, K., & Schippers, P. (2016). Frequency range of dust detection in space with radio and plasma wave receivers: Theory and application to interplanetary nanodust impacts on Cassini. *Journal of Geophysical Research: Space Physics*, *122*, 8–22. https://doi.org/10.1002/2016JA023081

Nesvorný, D., Janches, D., Vokrouhlický, D., Pokorný, P., Bottke, W. F., & Jenniskens, P. (2011b). Dynamical model for the zodiacal cloud and sporadic meteors. *The Astrophysical Journal*, *743*(2), 129. https://doi.org/10.1088/0004-637x/743/2/129

Nesvorný, D., Jenniskens, P., Levison, H. F., Bottke, W. F., Vokrouhlický, D., & Gounelle, M. (2010). Cometary origin of the zodiacal cloud and carbonaceous micrometeorites: Implications for hot debris disks. *The Astrophysical Journal*, *713*, 816–836. https://doi.org/10.1088/0004-637x/713/2/816

Nesvorný, D., Vokrouhlický, D., Pokorný, P., & Janches, D. (2011a). Dynamics of dust particles released from Oort Cloud Comets and their contribution to radar meteors. *The Astrophysical Journal*, *743*, 37. https://doi.org/10.1088/0004-637x/743/1/37

Odstrcil, D. (2003). Modeling 3D solar wind structure. *Advances in Space Research*, *32*, 497. https://doi.org/10.1016/s0273-1177(03)00332-6

Pantellini, F., Belheouane, S., Meyer-Vernet, N., & Zaslavsky, A. (2012). Nano dust impacts on spacecraft and boom antenna charging. *Astrophysics and Space Science*, *341*, 309–314. https://doi.org/10.1007/s10509-012-1108-4

Pokorný, P., Vokrouhlický, D., Nesvorný, D., Campbell-Brown, M., & Brown, P. (2014). Dynamical model for the toroidal sporadic meteors. *The Astrophysical Journal*, *789*, 25. https://doi.org/10.1088/0004-637x/789/1/25

Poppe, A. R., & Lee, C. O. (2020). The effects of solar wind structure on nanodust dynamics in the inner heliosphere. *Journal of Geophysical Research: Space Physics*, *125*, e28463. https://doi.org/10.1029/2020JA028463

Poppe, A. R., Lisse, C. M., Piquette, M., Zemcov, M., Horányi, M., James, D., et al. (2019). Constraining the solar system's debris disk with in situ *new Horizons* measurements from the Edgeworth-Kuiper belt. *The Astrophysical Journal Letters*, *881*(1), L12. https://doi.org/10.3847/2041-8213/ab322a

Pusack, A., Malaspina, D. M., Szalay, J. R., Bale, S. D., Goetz, K., MacDowall, R. J., & Pulupa, M. (2021). Dust directionality and an anomalous interplanetary dust population detected by the Parker solar probe. *Plant Science Journal*, *2*(5), 186. https://doi.org/10.3847/PSJ/ac0bb9

Quinn, P. R., Schwadron, N. A., Möbius, E., Taut, A., & Berger, L. (2018). Inner source C^+/O^+ pickup ions produced by solar wind recycling, neutralization, backscattering, sputtering, and sputtering-induced recycling. *The Astrophysical Journal*(98), 861. https://doi.org/10.3847/1538-4357/aac6ca

Rasca, A. O., Horányi, M., Oran, R., & van der Holst, B. (2014a). Modeling solar wind mass-loading in the vicinity of the Sun using 3-D MHD simulations. *Journal of Geophysical Research: Space Physics*, *119*, 18–25. https://doi.org/10.1002/2013JA019365

Rasca, A. P., Oran, R., & Horányi, M. (2014b). Mass loading of the solar wind by a sungrazing comet. *Geophysical Research Letters*, *41*, 5376–5381. https://doi.org/10.1002/2014GL060990

Rigley, J. K., & Wyatt, M. C. (2022). Comet fragmentation as a source of the zodiacal cloud. *Monthly Notices of the Royal Astronomical Society*, *510*, 837–857. https://doi.org/10.1093/mnras/stab3482

Rowan-Robinson, M., & May, B. (2013). An improved model for the infrared emission from the zodiacal dust cloud: Cometary, asteroidal and interstellar dust. *Monthly Notices of the Royal Astronomical Society*, *429*, 2894–2902. https://doi.org/10.1093/mnras/sts471

Schippers, P., Meyer-Vernet, N., Lecacheux, A., Belheouane, S., Moncuquet, M., Kurth, W. S., et al. (2015). Nanodust detection between 1 and 5 au using *Cassini* wave measurements. *The Astrophysical Journal*, *806*(1), 77. https://doi.org/10.1088/0004-637X/806/1/77

Schippers, P., Meyer-Vernet, N., Lecacheux, A., Kurth, W. S., Mitchell, D. G., & André, N. (2014). Nanodust detection near 1 AU from spectral analysis of Cassini/Radio and Plasma Wave Science data. *Geophysical Research Letters*, *41*, 5382–5388. https://doi.org/10.1002/2014GL060566

Schwadron, N. A., Geiss, J., Fisk, L. A., Gloeckler, G., Zurbuchen, T. H., & vonSteiger, R. (2000). Inner source distributions: Theoretical interpretation, implications, and evidence for inner source protons. *Journal of Geophysical Research*, *105*(A4), 7465–7472. https://doi.org/10.1029/1999JA000225

Schwadron, N. A., & Gloeckler, G. (2007). Pickup ions and cosmic rays from dust in the heliosphere. *Space Science Reviews*, *130*, 283–291. https://doi.org/10.1007/s11214-007-9166-6

Stark, C. C., & Kuchner, M. J. (2009). A new algorithm for self-consistent three-dimensional modeling of collisions in dust debris disks. *The Astrophysical Journal*, *707*, 543–553. https://doi.org/10.1088/0004-637x/707/1/543

Stenborg, G., & Howard, R. A. (2017). The evolution of the surface of symmetry of the interplanetary dust from 24° to 5° elongation. *The Astrophysical Journal*, *848*, 57. https://doi.org/10.3847/1538-4357/aa8ef0

Szalay, J. R., Pokorný, P., Malaspina, D. M., Pusack, A., Bale, S. D., Battams, K., et al. (2021). Collisional evolution of the inner zodiacal cloud. *The Planetary Science Journal*, *2*, 185. https://doi.org/10.3847/PSJ/abf928

Zaslavsky, A., Meyer-Vernet, N., Mann, I., Czechowski, A., Issautier, K., Le Chat, G., et al. (2012). Interplanetary dust detection by radio antennas: Mass calibration and fluxes measured by STEREO/WAVES. *Journal of Geophysical Research*, *117*, A05102. https://doi.org/10.1029/2011JA017480